International Forum on Aeroelasticity and Structural Dynamics
IFASD 2024
17-21 June 2024, The Hague, The Netherlands

THE EFFECT OF ASPECT RATIO VARIATION ON THE PRELIMINARY AEROELASTIC ASSESSMENT OF A MID-RANGE TRANSPORT AIRCRAFT

Matthias Schulze, Florian Müller*, Sunpeth Cumnuantip, Vega Handojo,
Tobias Hecken, Thomas Klimmek, Markus Ritter, Markus Zimmer

German Aerospace Center (DLR)
Institute of Aeroelasticity
Bunsentr. 10, 37073 Göttingen, Germany
matthias.schulze@dlr.de

Keywords: High Aspect Ratio Wing, Aspect Ratio Variation, cpacs-MONA, Aeroelasticity, Preliminary Design, Bell-Shaped Lift Distribution, Taper Ratio

Abstract: The wing aspect ratio (AR) is one of the main planform parameters to estimate the aerodynamic efficiency of a wing. A higher AR relates to a reduction in induced drag and consequently to an improved fuel economy. Since wings on civil transport aircraft are complex geometrical components with kinks, varying sweep, twist and dihedral angles over the span, mostly equipped with a heavy engine, the simplified assumptions made within the analytical formulations for wings conceptual design might be untrustworthy for modern aircraft with high AR wings. This paper evaluates the impact of the aspect ratio on the aeroelastic design of a medium-range transport aircraft using physics-based simulation at preliminary design stage. The research is conducted using the DLR-F25 configuration, developed in the German Aviation Research Program (*LuFo*-Project *VirEnfREI*). It features a baseline aspect ratio of *15.6*.

Since the AR of a wing is the ratio of the square of its span divided by its wing area, the AR can be varied in different ways. Within this paper, three different approaches to alter the AR are analyzed. All concepts utilize the same approach in which the center portion of the wing is kept constant until the kink. In this way, the wing-fuselage mount and the engine-wing integration is unaffected. Moreover, the leading-edge sweep angle has been kept unchanged to have comparable performance of the resulting aircraft. The baseline twist distribution at the corresponding sections of the wing is kept unchanged for the variants resulting in different lift distributions throughout the variations. Compared to other publications on the field of AR variations, where an increase of AR leads to an over-proportional ascending of wing-box mass, two variation approaches investigated in this paper show a passive load alleviation effect for higher AR leading to an even lower wing mass compared to the baseline wing. This effect is evoked by the bell-shaped spanwise lift distribution. These two variation methods result in a reduction in taper ratio with growing AR, accompanied in a reduction in wing mass. The third variation, on the other hand, increases in mass with respect to the AR, as the taper ratio is kept constant.

---

[*] *The results presented within this paper have been produced within the Master's Thesis of Florian Müller at the University of Liège, Faculty of Applied Sciences, in corporation with the German Aerospace Center (DLR), Institute of Aeroelasticity.*

1 INTRODUCTION

One of the main aims of the EU Flightpath 2050 [1] is to significantly reduce the fuel consumption of upcoming designs for transport aircraft. Besides the thrust specific fuel consumption, the structural mass and the lift-to-drag ratio of the aircraft are key factors in the reduction of the aircraft´s fuel consumption. Reducing drag is an essential challenge in aeronautics. The lower the drag of the wing, the better the fuel efficiency of the aircraft. The total drag of the wing is among others a combination of the profile drag, due to friction and pressure, and the induced drag, due to vortices at the wing tip. The latter represents a large part of the total drag and can be reduced by changing the wing planform in two different ways: On the one hand by ascending the Oswald factor and on the other hand by the increase in AR.

The Oswald factor is a correction factor that represents the change in lift induced drag of a wing compared with an ideal wing having the same aspect ratio and an elliptical lift distribution. The elliptical lift distribution leads to a minimum induced drag for a given lift and momentum of the lift force. That phenomenon has first been published by Prandtl in 1918 [2] for the case of a planar wing with a fixed span. This effect occurs for an unswept and untwisted wing, if the planform is formed as an ellipse. It can also be achieved by adapting the twist and profile characteristics among the wing span. In 1933 [3], Prandtl published the so called ‘bell-shaped’ lift distribution to be the minimum induced drag solution for a wing of constrained mass.

Phillips et. al. [4] presented analytical examples to minimize induced drag for rectangular wings with an optimum wing weight distribution. The induced drag can be reduced by about 16% compared to a fixed elliptical lift distribution under certain conditions.

Hunsaker et. al. [5] considered morphing wings to adapt the wing´s shape to get different lift distributions during steady level flight (*1g*) and maneuvering flight (*2.5g*). Figure 1 (left) represents the different lift distributions. The solid line represents a sample elliptic lift distribution at *1g*, minimizing the induced drag. The dashed line shows the same lift distribution at *2.5g*. This lift distribution also minimizes drag for the given lift coefficient and wingspan and is design driving for the wing structure. The dotted line represents Prandtl’s 1933 optimum lift distribution at *2.5g*. An optimized aircraft with various lift distributions for different flight points produced about 10% less drag over most of the mission profile compared to the baseline configuration.

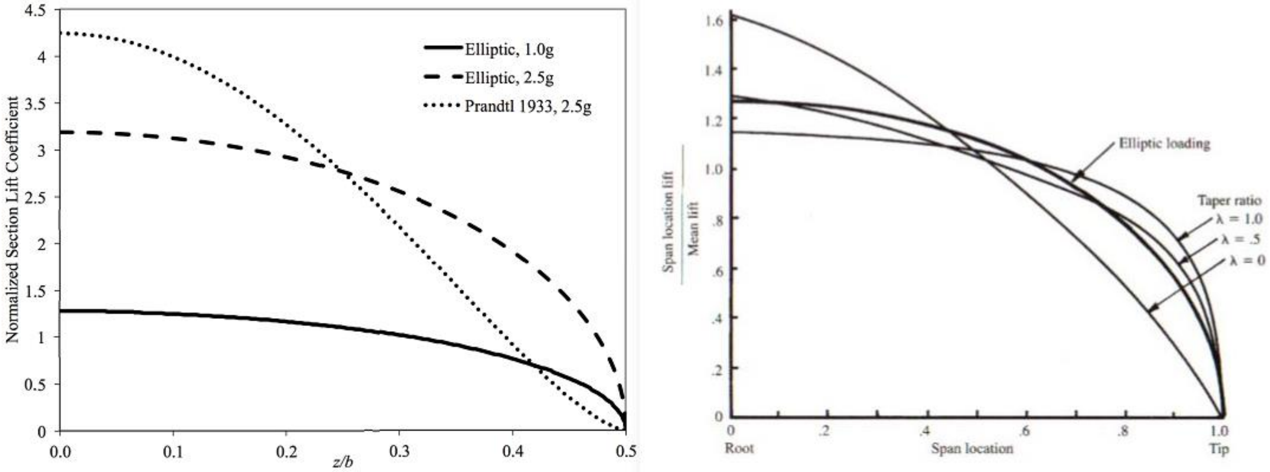

Figure 1: Different lift distributions among the half-span – elliptical vs. bell-shaped for different flight conditions (left) *[5]*; influence of wing taper ratio (right) *[6]*.

The right half of Figure 1 represents the effect of the taper ratio (wing tip chord divided by the wing root chord) on the lift distribution of a wing. A trend to a bell-shaped lift distribution is observed as the taper ratio diminish. It passively alleviates the bending moment by shifting the center of lift towards the wing root.

A relevant constraint in aircraft design is the wing root bending moment. It is a key characteristic for the wing's structural weight which counteracts the induced drag reduction. Drela [7] illustrated the bell-shaped tradeoff by comparing three load distributions ($\Delta\varphi$) for three different wing spans, each having the same lift and root bending moment (see Figure 2). By enlarging the span (b), the induced drag (D_i) reduces significantly compared to the baseline (b_1 and D_{i1}), even though the resulting load distributions are non-ideal compared to the elliptical lift distribution. The results from Hospodář et. al. [8] confirmed that optimized wings with bell-shaped lift distribution reach smaller drag coefficient values compared to other wings.

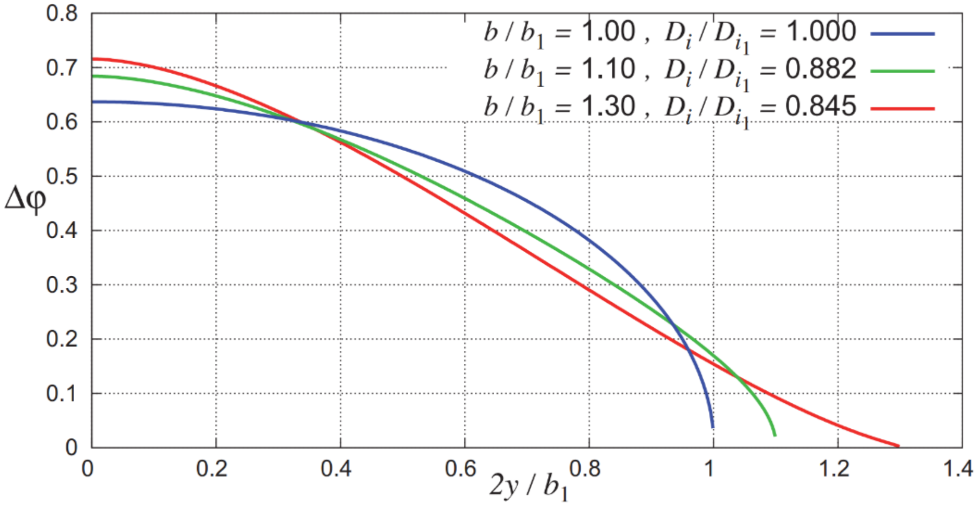

Figure 2: Optimum load distributions for three different wing spans having the same specified lift and root bending moment (*Figure 5.16 in [7]*).

The afore shown trend implies that an extension in span outweighs the deviation from the ideal Oswald factor representing the elliptical lift distribution. An increase in wing AR seems to be a promising lever in reducing the wing´s induced drag. Since AR is the ratio between the square of the span and the wing surface, the AR can be varied with different concepts.

Brooks et. al. [9] designed a modern, high AR variant for the NASA benchmark Common Research Model (CRM) by increasing the AR from *9* (baseline CRM) to an AR of *13.5* (CRM-13.5). The utilized multipoint optimization resulted in a design that achieved a 20% reduction in average fuel burn relative to the baseline design, while the total wing mass enlarges about 25%. In [10], Kennedy et. al. used more advanced future materials to enable the reduction in fuel burn while simultaneously diminishing the take-off gross weight for high aspect ratio wings.

Another interesting study regarding the aspect ratio variation of a wing including a non-linear beam model has been conducted by Calderon et. al. [11]. Results for the wing mass, lift-to-drag ratio and Breguet range for AR between *10* and 24 were compared between linear and non-linear beam model. The method used for aspect ratio variation was to keep the sweep, surface area, taper ratio and dihedral constant. A change in aspect ratio was achieved by increasing the span and reducing the root chord. As a result, the wing mass is ascending exponentially with the AR.

In [12], the conceptual design tool NeoCASS (Next generation Conceptual Aero Structural Sizing) was used to evaluate the effect of AR for a twin-aisle long-haul aircraft. Various aircraft models with different materials for the wing-box have been generated with growing wing aspect ratios. The AR variations have been generated by stretching the wing planform of a baseline aircraft, while keeping the wing area, leading edge sweep and taper ratio constant. All models revealed an ascending mass trend of the wing-box with an increase in AR.

To best account for the impact of aeroelasticity, for example effects like the structural deformations during maneuvers and flight, the dynamic behavior of the flexible structure during gust encounters, control reversal or even flutter, it is necessary to set up reliable structural models with physics-based simulations early in the design phase. These kinds of effects are especially important for the assessment of unconventional configurations like high AR wings. The aeroelastic structural design tool cpacs-MONA is capable of a fast generation of global Finite-Element-Models for complete aircraft configurations and will be introduced in the following chapter.

2 THE CPACS-MONA PROCESS

A basic aeroelastic structural design process can be defined by two steps: Firstly, the loads analysis of the flexible aircraft structure and secondly the structural design, using structural optimization methods considering aeroelastic constraints like sufficient control surface efficiency. Since the loads and structural properties are closely coupled, such process ought to run until convergence with respect to the structural weight and the loads is achieved. In order to ensure consistency of the simulation and optimization models for the loads analysis and the structural optimization, a specific parameterization concept has been developed at the German Aerospace Center (DLR) at the Institute of Aeroelasticity (DLR-AE) over the last 25 years. The computer program ModGen [13] has been developed to insure the previously mentioned consistency of the models. It sets up all necessary simulation and optimization models for the aeroelastic structural design process. Starting with ModGen, the basic aeroelastic structural design process at DLR-AE, named MONA is evolved. The name MONA is an acronym for the tool involved. It is at first the already mentioned computer program **Mo**dGen for the model set-up and MSC **Na**stran [14] as Finite-Element-Analysis (FEA) software of the loads analysis and the structural optimization.

The automatized process named cpacs-MONA [15] has been derived from the basic MONA process at DLR-AE to perform aeroelastic structural design for various aircraft configurations for the preliminary design using physics-based simulations. cpacs-MONA is integrated in DLR wide established design processes [16, 17, 18] or high-fidelity multi-disciplinary-optimization (MDO) chains [19, 20, 21, 22] using a Common Parametric Aircraft Configuration Schema (CPACS – [23]) dataset for data exchange. cpacs-MONA is built modularly, is written in Python code and extracts the information about the aircraft from the CPACS dataset. CPACS describes a wide range of aircraft characteristics like the outer geometry (profiles and segments), the global aircraft parameters, the topology of the inner structure, the engine outer shape, and much else. Besides, the aircraft information, processed information like aerodynamic data, aircraft loads, detailed mass distribution for each component, together with tool parameters can be stored in the CPACS dataset. cpacs-MONA automatically reads out the information about the wing planform, the wing inner topology and initial component thicknesses together with the engine, pylon, and landing gear positions and dimensions. It also uses information about aircraft masses like design, primary and secondary masses plus the dimensions of the control surfaces, and the borders of the fuel tanks. With this information, cpacs-MONA creates suitable input-files for the involved modules. For

ModGen, each component (wing, horizontal and vertical tail, fuselage) is built separately and executed in parallel. All components are combined to the GFEM/Dynamic. GFEM stands for global finite element model, and dynamic expresses the applicability of the model for structural dynamic analysis. Furthermore, the MSC Nastran simulations like the static aeroelastic trim analysis, the dynamic gust analysis or the structural optimization analysis can each be executed in parallel within the individual steps. Besides the already mentioned modules, cpacs-MONA combines many modules written in different programming languages forming an automated process flow as highlighted in Figure 3.

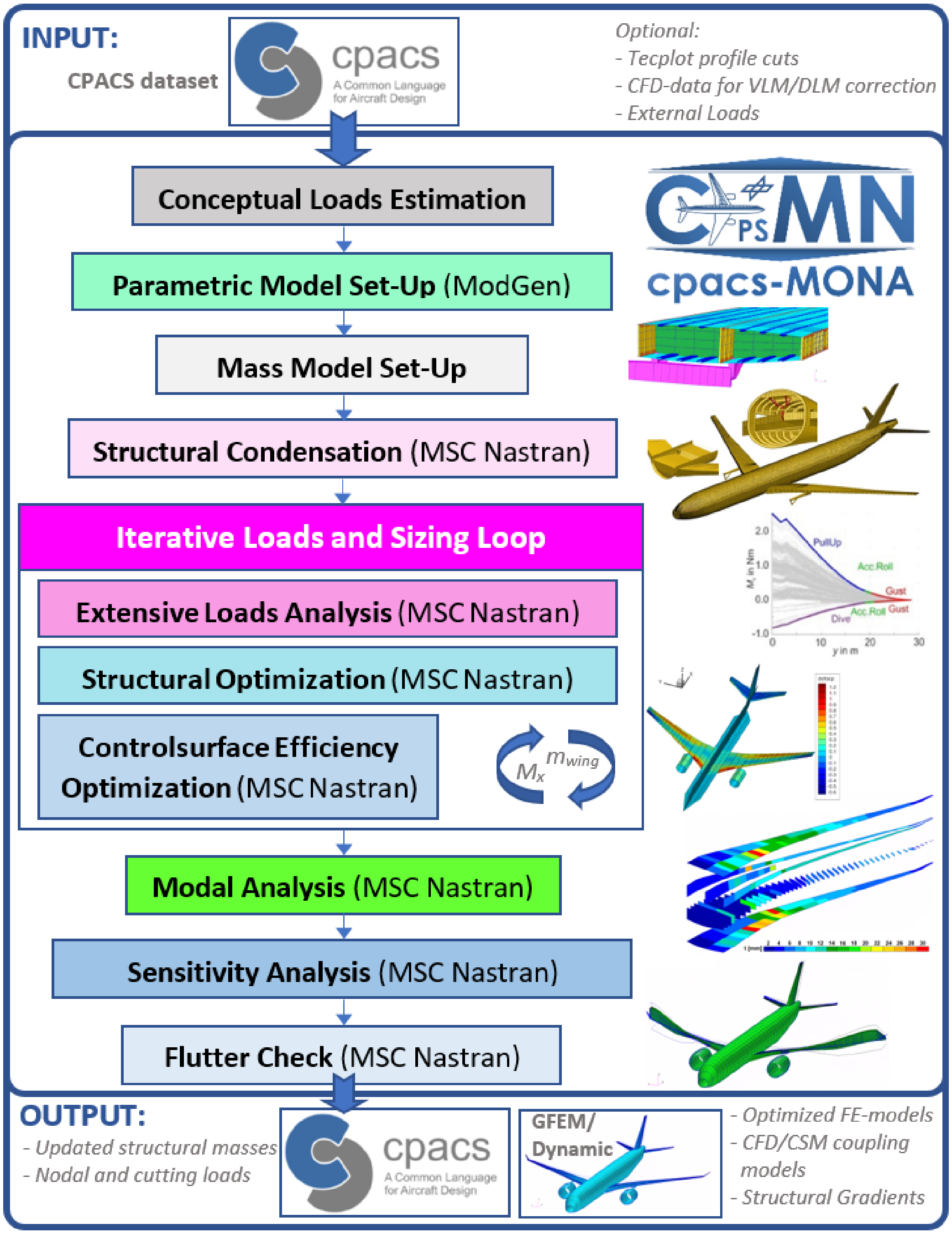
INPUT:
CPACS dataset
cpacs
A Common Language for Aircraft Design
Optional:
- Tecplot profile cuts
- CFD-data for VLM/DLM correction
- External Loads
Conceptual Loads Estimation
Parametric Model Set-Up (ModGen)
Mass Model Set-Up
Structural Condensation (MSC Nastran)
Iterative Loads and Sizing Loop
Extensive Loads Analysis (MSC Nastran)
Structural Optimization (MSC Nastran)
Controlsurface Efficiency Optimization (MSC Nastran)
M_x
m_{wing}
Modal Analysis (MSC Nastran)
Sensitivity Analysis (MSC Nastran)
Flutter Check (MSC Nastran)
cpacs-MONA
2.0
1.0
0.0
-1.0
M_x in Nm
PullUp
Acc.Roll
Gust
Dive
Acc.Roll
Gust
0
10
20
30
y in m
OUTPUT:
- Updated structural masses
- Nodal and cutting loads
cpacs
A Common Language for Aircraft Design
GFEM/
Dynamic
- Optimized FE-models
- CFD/CSM coupling models
- Structural Gradients

Figure 3: Process flow of the automated aeroelastic structural design process cpacs-MONA.

The process starts with an estimation of preliminary loads based on conceptual design methods according to [24], followed by an estimation of a generic beam model representing the fuselage stiffness. The conceptual loads are used for a preliminary cross-section sizing (PCS) within ModGen [25]. Due to the PCS, a more realistic wing representative with respect to the shell thickness distribution and bar properties is provided. As shown in Figure 4, the wing ribs, spars, and skins are modeled with shell elements. The other wing component structures like the spar caps, the inner reinforcement structure, or the stringers are modeled with bar or beam elements. A parametric elastic pylon model is also available to account for the elastic interaction of the engine with the wing and vice versa.

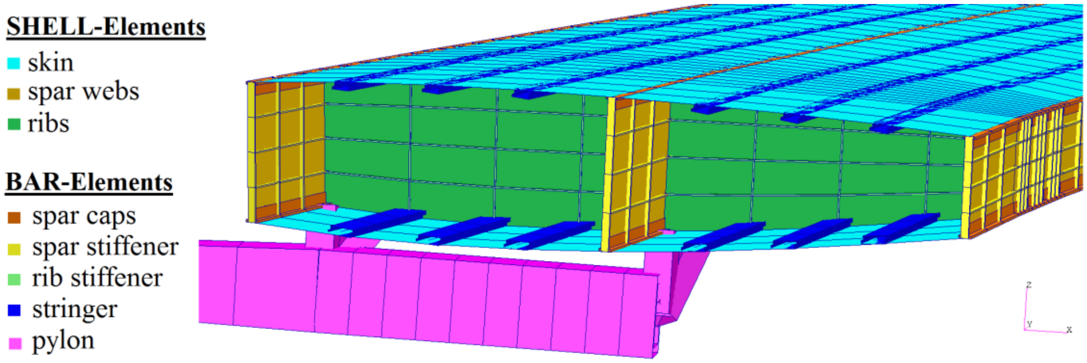

Figure 4: Wing topology of the FE-models highlighting the applied structural elements.

For a conclusively substantiated aeroelastic analysis, reasonable mass models have to be composed. A mass model module reads out the mass-breakdown for each component and creates a model with distributed mass and inertia entities in line with the given geometrical space of the individual component. The fuel tank is calculated according to the geometrical borders (such as ribs and spars) as defined in CPACS. The masses of the engine and landing gear are extracted from the CPACS dataset and converted into Nastran *CONM2* elements. The resulting operating empty mass (OEM) together with defined combinations of fuel and payload/passenger masses form the design masses and different mass cases which are important for the loads analysis of the aircraft.

To reduce the complexity of the GFEM/Dynamic for the extensive loads analysis, the stiffness of the structural model is condensed to the loads reference axis (*LRA*) points. Such condensed model is set up by ModGen using the Guyan reduction [26]. This model has the same dynamic characteristic (mass and stiffness) as the full GFEM/Dynamic but much less degrees of freedom.

For this paper, hundreds of static load cases according to the regulations *CS25.335* [27] containing symmetrical pull-up and push-down maneuvers, yawing and rolling maneuvers together with 1g-level flight loads paired with dynamic gust encounters are simulated for each wing configuration with four different mass cases of the aircraft. For the steady maneuvers, MSC Nastran Solution 144 is used and Solution 146 for the dynamic gust simulations [28]. In context of the *2.5g* pull-up maneuvers, the inner ailerons are symmetrically deflected to alleviate the maximum loads according to [29]. The load cases with the maximum and minimum cutting moments for bending and torsion as well as forces for shear are selected for each wing-like component. The forces and moments acting on the primary structure of these load cases are extracted and used for the structural optimization of the wing-like components.

MSC Nastran Solution 200 [30] is used for the structural optimization. The optimization model consists of the definition of design variables, constraints, and an objective function. The objective function for the structural optimization is the wing-box mass to be minimized under consideration of aeroelastic constraints like control surface efficiency, allowable strain values for composite materials or stress limits for metallic materials per shell element. As design variable, the thicknesses of the shell elements for the load-carrying wing structures can be adjusted to fulfill the objective function. The design variables are combined to design regions to reduce the complexity of the optimization task.

The loads analysis and structural optimization are conducted iteratively, while the mass and the stiffness of the simulation models are updated at each step until the mass and the loads of the aircraft configuration converge. This degree of process automatization emphasizes that cpacs-MONA does not only generates different simulation models for different AR variations to evaluate the individual influence on the loads or on the structural mass. To a greater degree, it optimizes the load-carrying wing structure of each aircraft configuration in an iterative loads and structural optimization loop to best bear the loads emerging on the different AR variations. At the end of the convergence loop, additional analysis like flutter or sensitivity analysis can be performed within cpacs-MONA according to the purpose of the output of the process.

3 BASELINE AIRCRAFT CONFIGURATION

This chapter focuses on the main characteristics of the initial baseline configuration. The simulation models used to evaluate the results of the AR variation will be presented in detail. For a point of reference, the main results of the performed simulations will be examined in a greater detail for the baseline aircraft configuration.

The DLR-F25 configuration developed within the German Aviation Research Program (*LuFo*-Project *VirEnfREI* [31]) is used as baseline for the performed AR variation. The results are from the preliminary design phase while the development of the configuration is still ongoing. The DLR-F25 is a single-aisle medium-range aircraft configuration for about 240 passengers and has a fuselage length of *44.51 m*. The initial AR of *15.6* of the DLR-F25 main wing is considerably high compared to contemporary aircraft configurations like the Airbus A321-100 with an AR of *9.4* [32]. The Top Level Aircraft Requirements (TLARs) derived from the overall aircraft design (OAD) for the DLR-F25 are partially highlighted in Table 1.

Table 1: Top Level Aircraft Requirements for the DLR-F25 baseline configuration.

Aircraft Parameter	Value
Operating Empty Mass	47 t
Max. Take-off Mass	86 t
Max. Payload	25 t
Design Cruise Mach	0.78
Design Range	2500 NM
Max. Operating Altitude	FL 400

3.1 Geometry

The outer geometry of the DLR-F25 is shown in Figure 5. It is equipped with two ultra-high bypass-ratio turbofan engines with a bypass-ratio of *13.8:1*, mounted under the wing. Each engine has an outer diameter of *2.78 m* and a dry-mass of *2630 kg*. One special characteristic about the DLR-F25 is the fuselage mounted main landing gear.

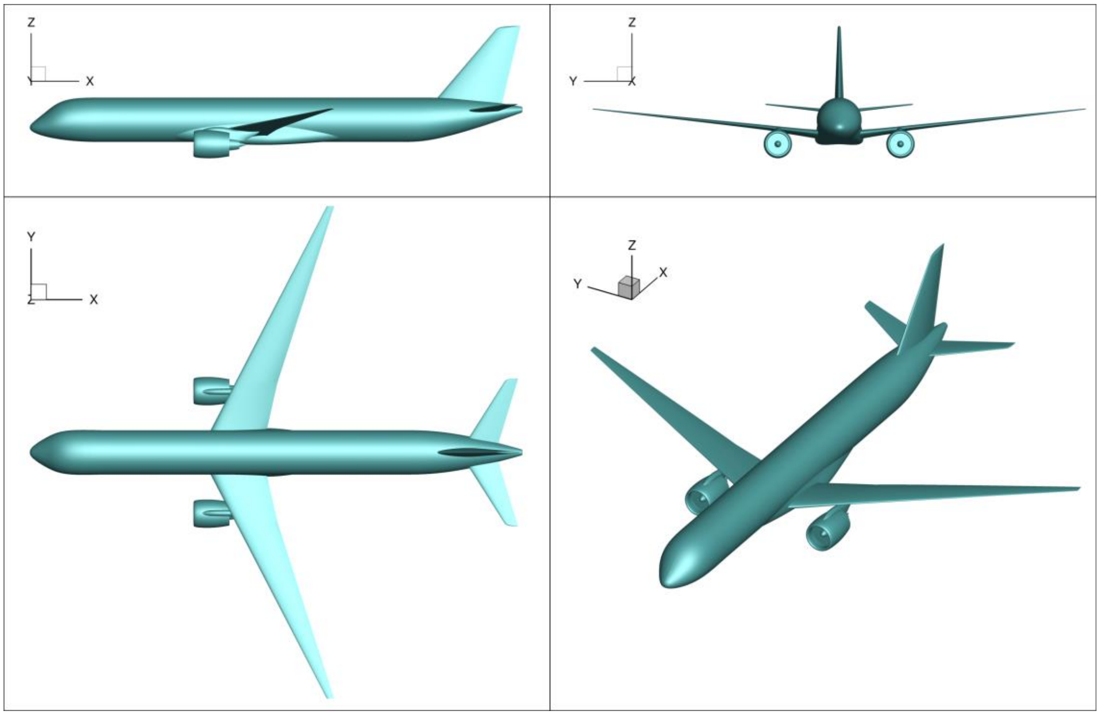

Figure 5: Outer geometry of the DLR-F25 baseline configuration derived from CPACS.

The wing planform is shown in Figure 6. The wing is divided into 5 sections: *center*, *root*, *kink*, *mid* and *tip*. A design feature of the DLR-F25 main wing is the folding wing tip installed at *18 m* (mid-section) of the wing semi-span. This location is selected to fit into the *36 m* regulations of the ICAO Aerodrome Reference Code C categorizing the aircraft´s wingspan at the airport.

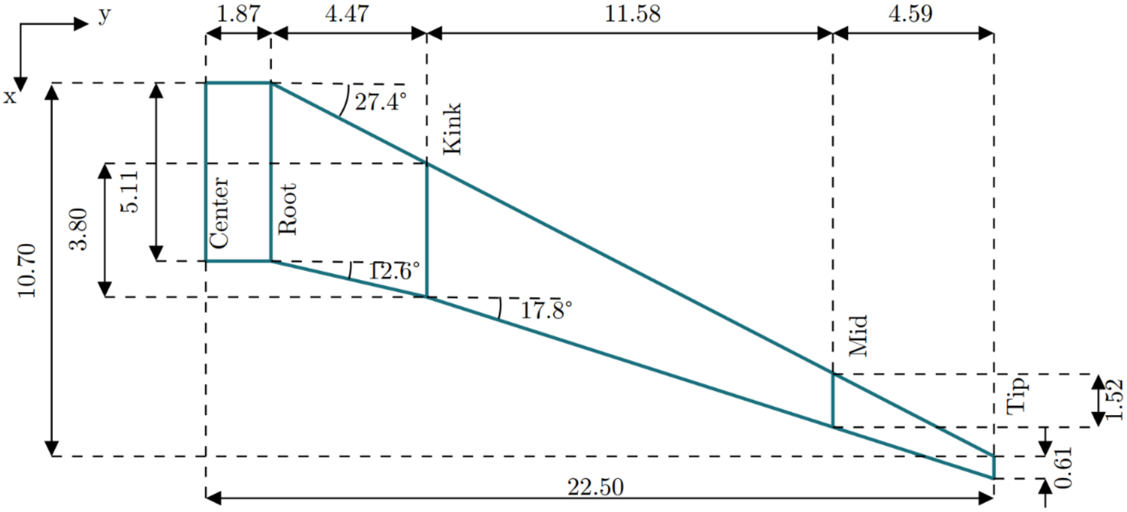

Figure 6: Baseline planform devided into five sections (dimensions in meter).

The key planform characteristics of the DLR-F25 main wing are presented in Table 2. Compared to the Airbus A321-100, the DLR-F25 wing more slender having a 17% lower mean aerodynamic chord (MAC) and half the taper ratio [32]. The main parameters describing the aerodynamic characteristics of the main wing are listed in Table 3 for each section. The negative twist at the tip section is used to strengthen the washout-effect [33] to passively reduce the wing-root bending moments by shifting the aerodynamic forces from outboard to inboard to reduce its momentum.

Table 2: Key planform parameters for the main wing of the DLR-F25 baseline configuration.

Parameter	Main Wing
Area	130.1 m^2
Span	45 m
Aspect Ratio	15.6
Taper Ratio	0.12
MAC	3.54 m

Table 3: Main aerodynamic characteristics for the main wing of the DLR-F25 baseline configuration per section.

Wing Section	Dihedral [deg.]	Rel. Profile Thickness [%]	Twist [deg.]
Center	0.0	14.06	3.0
Root	0.0	14.06	3.0
Kink	8.3	11.77	1.5
Mid	6.4	11.32	0.78
Tip	6.4	10.88	-1.0

The ribs are located between the front and rear spar and have a spacing of approximately *70 cm*. That leads to 36 ribs for the baseline wing. An illustration of the rib distribution and the spar positions is shown in Figure 7. The folding mechanism of the wing tip is insinuated by the streamwise rib (rib no. 28) in the outer section of the wing.

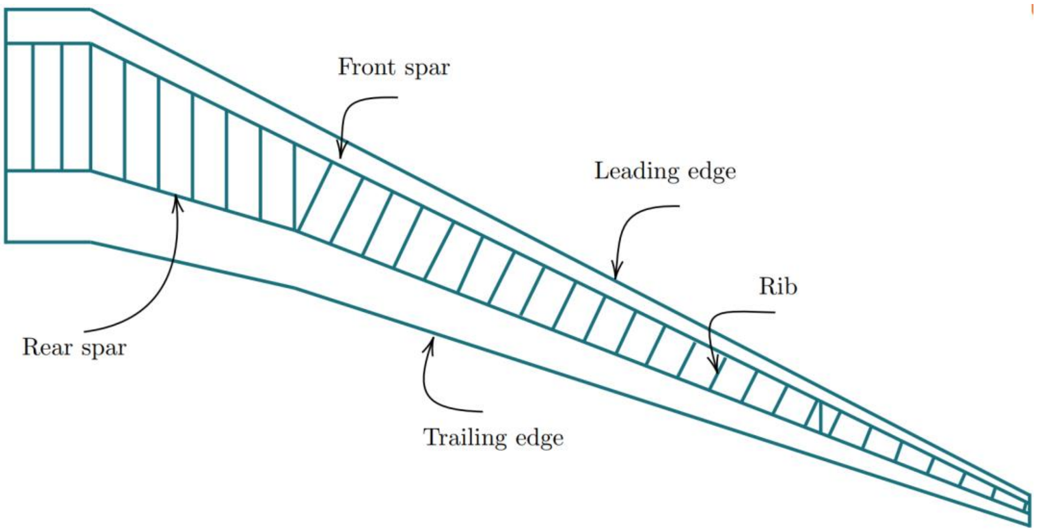

Figure 7: Schematic visualization of the wing inner structure of the baseline configuration.

3.2 Simulation Models

To perform a conclusively substantiated aeroelastic assessment, suitable simulation models for the FEA-software have to be set up. Structural FE-models represent the stiffness of the airframe and aerodynamic panel models depict the aerodynamic forces. Reasonable mass models inducing the inertia loads.

3.2.1 Structural Model

cpacs-MONA builds up the structural models of an aircraft configuration using the model generator ModGen. The full model of the DLR-F25 consists of approximately 13.850 FE-nodes and 33.100 Finite Elements and form the GFEM/Dynamic. To reduce the computational effort for the extensive load analysis of the flexible aircraft, the GFEM/Dynamic is condensed. The condensed model correspondingly consists solely of 370 FE-nodes forming the stiffness matrix. *RBE2*-elements and corresponding nodes are used for the aeroelastic coupling of the structural and the aerodynamic model. Spline elements transfer the forces and motions between the two models. Both models of the GFEM are visualized in Figure 8. The shell elements of the fuselage and engine nacelle are for illustrational purpose.

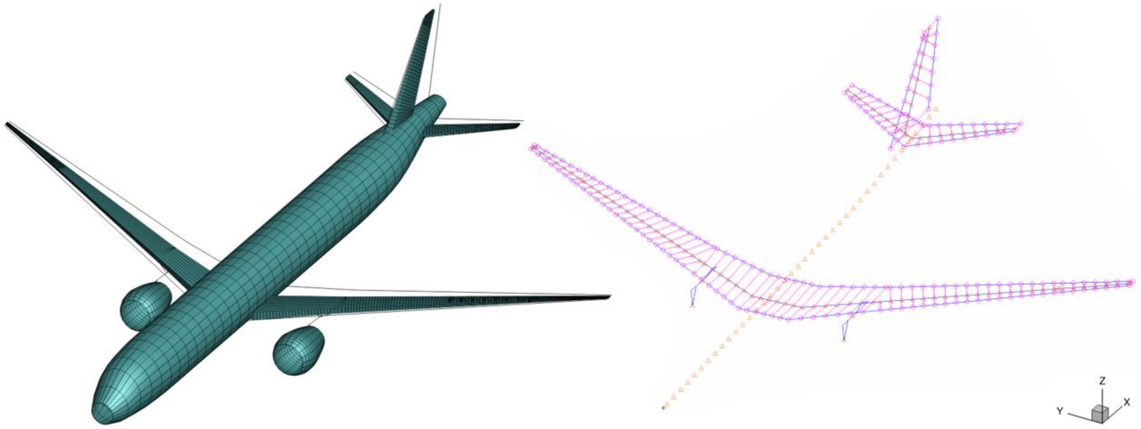

Figure 8: GFEM/Dynamic of the DLR-F25 baseline configuration – full model (left); condensed model used within the load analysis (right).

The composite material properties used for the load-carrying shell elements are listed in Table 4. The composite name implies the percentage ply dissemination of the laminate. The name *'60_30_10'* means, that 60% of the composite composes of 0°-plies, 30% of 45°-plies and 10% of plies have an orientation of 90° and '*20_60_20*' correspondingly starting with 0°, followed by 45° and 90°. Each ply is made of the material with the name 'T800_M21_268gsm' comprising the following properties:

$$E_{11} = 1.53e11\ N/m^2; \quad E_{22} = 8.50e9\ N/m^2; \quad G_{12} = 4.20e9\ N/m^2; \quad \rho = 1580\ kg/m^3$$

E_{11} and E_{22} are the direction depending modulus of elasticity, G_{12} the shear modulus and ρ is the material density. The upper and lower skin covers are modeled with the '*60_30_10*' composite. The spar webs and ribs are modeled using the '*20_60_20*' composite.

Table 4: Material definition of the shell elements according to MSC Nastran *MAT2* convention.

Composite Name	**Direction**	**G11 [N/m^2]**	**G12 [N/m^2]**	**G13 [N/m^2]**	**G22 [N/m^2]**	**G23 [N/m^2]**	**G33 [N/m^2]**	**ρ [kg/m^3]**
'60_30_10'	Membrane	1.07e11	1.35e10	1.09e10	3.44e10	1.09e10	1.47e10	1580
	Bending	8.31e10	2.60e10	2.39e10	3.35e10	2.39e10	2.72e10	1580
'20_60_20'	Membrane	6.03e10	2.40e10	2.18e10	6.03e10	2.18e10	2.52e10	1580
	Bending	5.21e10	3.57e10	3.40e10	4.51e10	3.40e10	3.69e10	1580

To set up the composite model, first the material properties defined in the CPACS-dataset are extracted. The available data provides stacking sequences of each component and material properties of each ply. The composite lay-up consists of symmetric laminates with *[0°, ±45°, 90°]* plies. As next step, the transformation of the ply material properties to compounded laminate properties is done by the formulation of the *ABD*-matrices. *'A'* represents the in-plane stiffness matrix, *'D'* the bending stiffness matrix and *'B'* the coupling stiffness matrix. For symmetric laminates, the coupling matrix is equal to zero. The coupling terms in correlation to Table 4 are *G12*, *G13* and *G23*. These terms are not negligible in comparison to the main stiffness representatives *G11*, *G22* and *G33*. This is an indicator, that the defined laminate is unbalanced.

3.2.2 Mass Model and Longitudinal Stability

The generated mass cases used within the loads analysis have an internal ID. This ID together with the percentage indication of the payload and fuel compositions are listed in Table 5.

Table 5: Investigated Mass Cases listing the corresponding fuel and payload conditions.

	MOOee	**MFOeF**	**MZOAe**	**MTOAa**
Design Mass	OME	'delivery'	MZFM	MTOM
Mass [t]	50.4	69.3	75.4	86.0
Payload [%]	0	0	100	100
Payload [t]	0	0	25	25
Fuel [%]	0	100	0	56
Fuel [t]	0	18.9	0	10.6

The stability margin is important in order to ensure the longitudinal (or pitching) stability of the aircraft. It is expressed as:

$$K_n = \frac{x_{AC} - x_{CG}}{MAC} = -\frac{dC_m}{dC_L}$$

With x_{AC} the x coordinate of the aircraft's aerodynamic center, x_{CG} the x location of the center of gravity, C_m the pitching moment, C_L the wing lift coefficient and *MAC* the mean aerodynamic chord. This margin has to be positive for a stable aircraft. In general, it should range from 5% to 40% [34]. The center of gravity, aerodynamic center and stability margin of the elastic aircraft for each mass cases are listed in Table 6.

Table 6: Aircraft stability parameters for steady level flight for the different mass cases.

	MOOee	**MFOeF**	**MZOAe**	**MTOAa**
x_{CG} [m]	20.40	20.75	20.05	20.05
x_{CG} [$\%_{MAC}$]	25	35	15	15
x_{AC} [m]	21.33	21.26	21.31	21.29
K_n [%]	26.3	14.4	35.6	35.0

3.2.3 Loads Model

The automatically generated aerodynamic model is shown in Figure 9. This model consists of macro panel elements for the vortex and doublet lattice method (VLM [35] and DLM [36]). Within the elastic trim analysis, the macro panels of the wing-like structures are geometrically modified to account for the camber and twist effects of the wing. Aerodynamic corrections to account for compressibility effects have not been considered within this publication. The control surfaces like elevator, rudder, and aileron are also defined within the aerodynamic model according to their definition within the CPACS dataset. There is no structural modelling of the control surfaces.

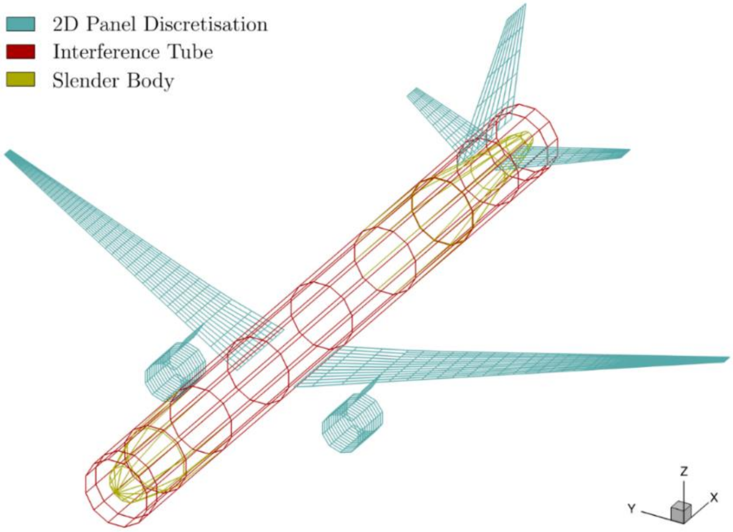
2D Panel Discretisation
Interference Tube
Slender Body
Z
Y
X

Figure 9: Aerodynamic model for the GFEM of the DLR-F25 using VLM/DLM panels.

To select the load cases for the structural optimization, so-called load envelopes are generated for a set of monitoring stations. The basis of the envelopes are pairs of cutting loads which are built for each load case and combined into a diagram. The envelope is the resulting convex-hull formed around all load cases. Within cpacs-MONA, cutting moments for torque (M_y), shear (F_z), and bending (M_x) are considered for each wing-like component. Figure 10 illustrates the load monitoring station used within this publication to compare the loads for the different AR variations.

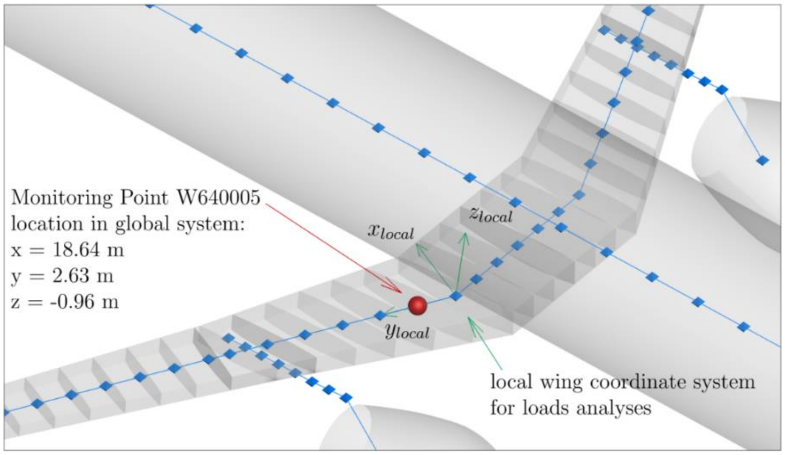
Monitoring Point W640005
location in global system:
x = 18.64 m
y = 2.63 m
z = -0.96 m
x_{local}
z_{local}
y_{local}
local wing coordinate system
for loads analyses

Figure 10: Location and coordinate system of the monitoring station used for the two-dimensional cutting load evaluation of the DLR-F25 baseline configuration.

3.2.4 Aerodynamic Performance Calculation

The main aerodynamic characteristics of an aircraft are the lift (*L*) and the drag (*D*). Since the outcome of VLM is a delta in the pressure coefficient (Δc_p) per lifting panel, the Δc_p can be used to calculate the lift and drag coefficients. The lift generated by an aircraft is given by:

$$L = \frac{\rho}{2} \cdot {V_\infty}^2 \cdot C_L \cdot S$$

with ρ the air density, V_∞ the airspeed, C_L the lift coefficient and *S* the wing reference area. This represents the main part of the total lift that balances the aircraft mass in 1g-level flight. The induced drag is the drag share due to lift, since the high pressure on lower wing surface and the low pressure on the upper surface induces vortices at the tips of a wing. The induced drag is proportional to the square of the lift coefficient, so that its coefficient ($C_{D,i}$) can be calculated as followed:

$$C_{D,i} = \frac{{C_L}^2}{\pi \cdot e \cdot AR}$$

with *AR* the aspect ratio and *e* the Oswald (or efficiency) factor. The lift coefficient along the span can be extracted as output of the Nastran Solution 144 trim analysis. The total wing lift coefficient has to be computed. C_L is the integral of the lift coefficient along the span by considering the local chord length. It is expressed as:

$$C_L = \frac{1}{S} \int_{-b/2}^{b/2} c_l(y) \cdot c(y) dy$$

where *S* denotes the surface area of the wing, *b* the wing span, c_l the local profile lift distribution and *c* the local chord length. To compute the Oswald factor, several concepts can be used. The concept used for this estimation is a numerical approximation directly based on the lift distribution as described by Anderson [37]. This method uses a Fourier sine series with the general circulation distribution Γ as shown in the following equation:

$$\Gamma(\theta) = 2 \cdot b \cdot V_\infty \cdot \sum_{n=1}^{N} A_n \cdot \sin n\theta$$

where the A_n coefficients are unknowns. The circulation can be expressed as:

$$\Gamma(\theta) = \frac{L'(\theta)}{\rho_\infty \cdot V_\infty}, \qquad with \quad y = \frac{b}{2} \cdot \cos\theta$$

The first coefficient A_1 can be determined from the total wing lift coefficient and it represents the elliptical lift distribution ($e=1$):

$$A_1 = \frac{C_L}{\pi \cdot AR}$$

The following system of equations needs to be solved in order to find the other A_n coefficients:

$$\Gamma'^{(\theta)} - A_1 \cdot \sin n\theta = 2 \cdot b \cdot \rho_\infty \cdot {V_\infty}^2 \cdot \sum_{n=2}^{N} A_n \cdot \sin n\theta$$

If the A_n coefficients are known, the Oswald factor is obtained according to Anderson [37]:

$$e = \frac{1}{1+\delta}, \qquad with\ and \quad \delta = \sum_{n=2}^{N} n\left(\frac{A_n}{A_1}\right)^2$$

3.2.5 Structural Optimization Model

The objective function for the structural optimization is the wing-box mass to be minimized under consideration of aeroelastic constraints like control surface efficiency or allowable stress or strain values per shell element. As a design variable, the thicknesses of the shell elements from the load-carrying wing structure can be adjusted to fulfill the objective function. The design variables are combined to design regions to reduce the size of the optimization task. The design regions of the wing-box are the partial skin surfaces, surrounded by spars and ribs, and the partial rib and spar surfaces due to their intersections among each other. Since the wing-box of the DLR-F25 main wing consists of 36 ribs and two spars, the optimization model consequently has 36 design variables for the ribs, 70 for the skin covers, and altogether 70 for the spars. In total, 176 design variables are optimized to minimize the wing-box mass of the main wing per optimization step. The dimensions of the reinforcement bar elements are not part of the optimization task and are modelled using aluminum material definition. For the optimization of the composite materials, the lamination parameters are kept unchanged throughout the optimization procedure and micromechanical effects of the composite material are ignored. The design responses are chosen to be the principal strains and shear strain and are defined to be *3500* microstrains (*μm/m*) for compression and *4000* microstrains for tension [38]. Buckling of the composite wing components such as the skin, spar or rib webs is not yet implemented in the automated design process.

The structural optimization within cpacs-MONA is conducted in two steps. The first step uses the simulated loads to optimize the structure to withstand the loads at each flight point. For the second step, the resulting structural thicknesses from the first step are defined to be the lower bound of the design variables. Within the second optimization step, only the aileron efficiency is the constraint to ensure sufficient roll-control for each configuration.

3.3 Baseline Results

Within this paper, an aeroelastic assessment of different AR variations is performed. To get a better understanding for the effect of the AR on the results, the baseline results will be shown in more detail in the following sub-paragraphs. A special attention is turned on the loads, the resulting structural properties, followed by the aerodynamic performance of the baseline configuration.

3.3.1 Loads

To reduce the computational effort of the optimization task, a component-wise load case selection is performed. Like mentioned in chapter 3.2.3, a convex-hull is computed around pairs of cutting loads for the shear forces, the bending and torsional moments, forming the load envelopes for a selected number of monitoring stations. The forces and moments of these load cases are extracted and afterwards used for the structural optimization of the wing-like components.

Within Figure 11, the two-dimensional wing cutting load envelope is visualized for the bending moment (M_x) and the torsional moment (M_y). Since the load cases forming the convex hull (most outer points) are indicated with their internal load case IDs, it can be seen, that the maximum and minimum (most negative) torsional moment are caused by the mass case *MTOAa* with a pull-up

(*LLFPU*) and a push-down (*LLFPd*) maneuver, respectively. The gust cases are less dominant at the location of the monitoring point W640005 near the wing root, but they become more relevant at the outer section of the wing.

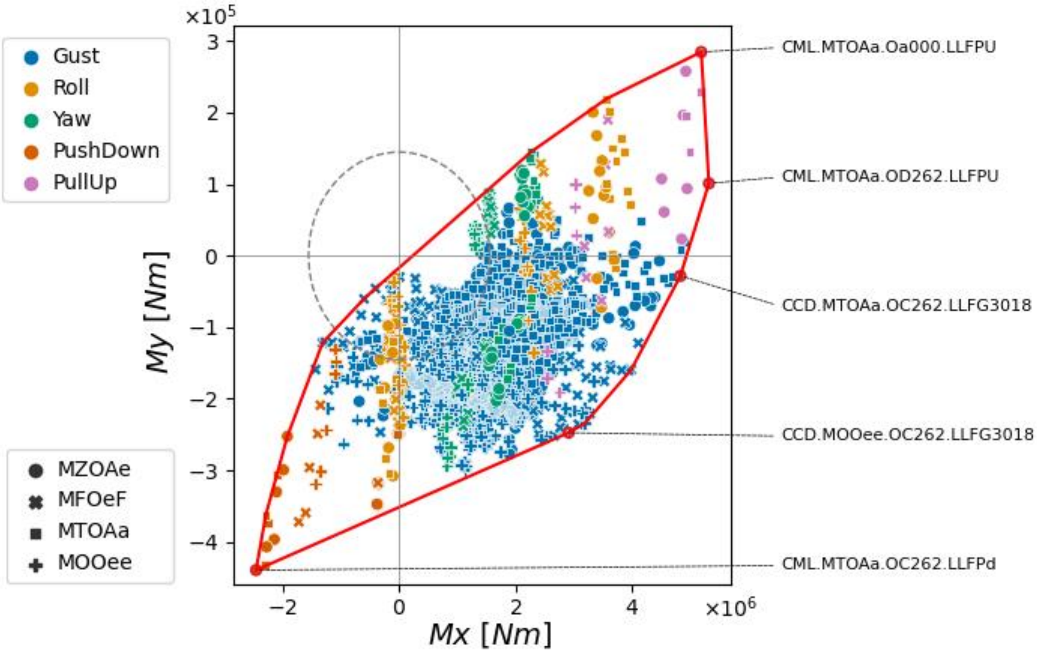

Figure 11: Wing cutting load envelope for the bending moment (M_x) and the torsional moment (M_y) of the monitoring station W640005 (see Figure 10).

3.3.2 Structural Properties

To withstand the loads acting on the primary wing structure, the thickness of the design variables for the upper and lower skin covers, the ribs and the spar webs are adjusted by the MSC Nastran Solution 200 optimization algorithm. The resulting thickness distribution for the baseline configuration of the DLR-F25 is highlighted in Figure 12.

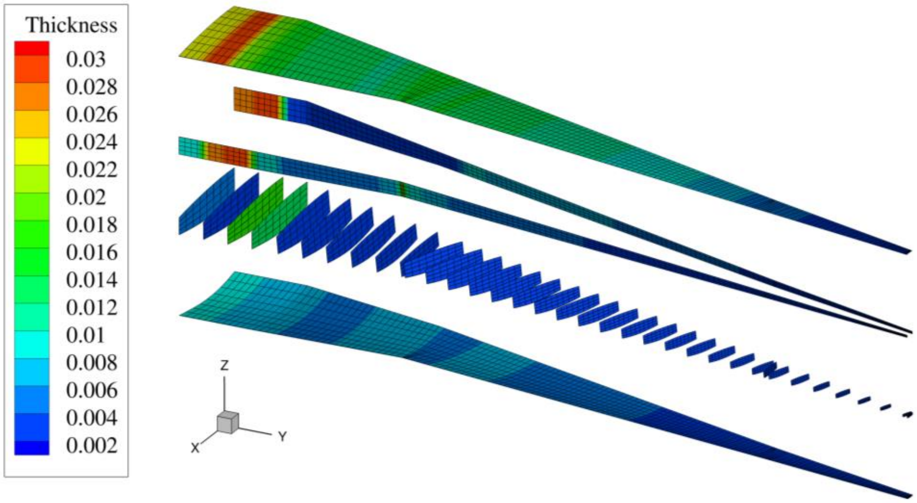

Figure 12: Thickness distribution of the load-carrying structure for the main wing – exploded view of the ribs, spars and skin covers (dimensions in meter).

The wing primary mass is the resulting mass of the FEM-optimization (sized mass) factorized with a so-called mass penalty to account for non-ideal weight penalties for the wing according to [34]. This mass penalty is due to the fact, that the sized mass of the FE-Model does not reflect the real mass of the primary wing structure. The thickness distribution on the one hand influences the mass of the structure and on the other hand it's elasticity. To get an insight of the wing's elasticity, the bending and twist deformations over the wing span within the steady level flight of the different mass cases is displayed in Figure 13.

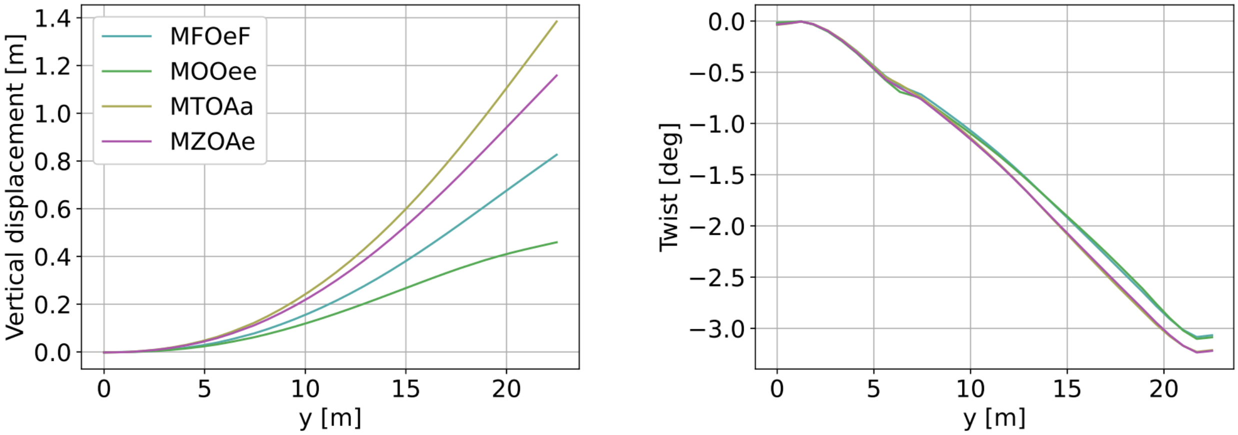

Figure 13: Vertical displacement and twist deformation along the wing span for the four different mass cases in steady level flight within the local coordinate system of the LRA.

The highest wing bending is observed for the heaviest mass case representing the maximum take-off-weight. Since the wing stiffness is the same for each mass case, the wing needs to generate more lift for the heaviest mass case which means more vertical force and consequently more vertical displacement. At this phase of the development, the maximum wing bending represents 6% of the half span. The results for the twist deformation along the span are alike for each mass case. Due to the washout-effect, the bending and twist deformations are coupled and have therefore an impact on each other.

The wing stiffness and mass distribution do not have only an impact on the deformation of the wing during flight, it also influences the structural dynamic behavior. Within Table 7, the most relevant elastic wing Eigenmodes for the aeroelastic assessment are presented. Since the wing of the DLR-F25 has a high AR and a small taper ratio, the 1st symmetric wing in-plane bending mode occurs before the torsional mode.

Table 7: Most relevant elastic wing Eigenmodes for the OEM mass case of the DLR-F25 baseline configuration.

Mode No.	**Eigenmode**	**Frequency**
7	1st sym. wing out-of-plane bending	2.41 Hz
18	1st sym. wing in-plane bending	6.71 Hz
30	1st sym. wing torsion	17.92 Hz

3.3.3 Aerodynamic Performance

A sufficient lift distribution approximation according to chapter 3.2.4 can be obtained by taking three values of the lift among the span: one at the root, one in the middle of the wing and one at the tip. Since the lifting surfaces of the wing ends at the fuselage, the wing lift distribution needs to be extrapolated to the symmetry plane. The Nastran extracted, the approximated and the exemplary elliptical lift distributions of the wing are shown in Figure 14 for the *MOFeF* mass case of the DLR-F25 baseline configuration. The resulting lift distribution shows the trend of the bell-shape. The already quite low value of the taper ratio of *0.12* for the baseline configuration can lead to the resulting lift distribution. The Oswald factor for the baseline is *0.84* and the induced drag coefficient results in *0.00146*.

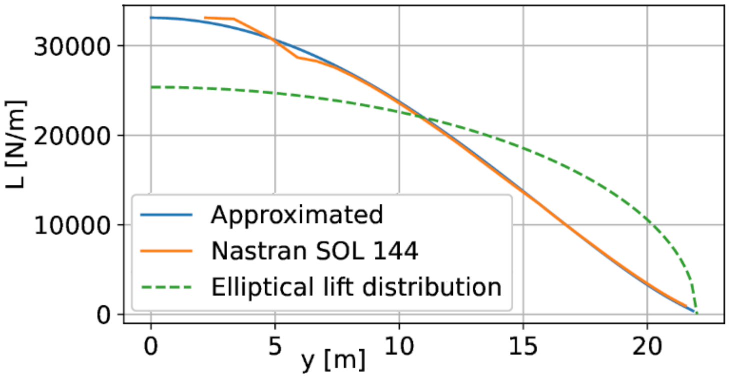

Figure 14: Lift distribution along the wing span of the *MFOeF* case during steady level flight.

4 ASPECT RATIO VARIATION

The objective of this chapter is the investigation of the effect of the AR variation on the main aircraft characteristics. It starts with a description of the three different concepts used for the AR variation. As follows the effect on the in Chapter 3 presented results of the baseline configuration are discussed. All results are extracted after convergence of loads and mass was achieved.

4.1 Methods of Aspect Ratio Variations

Within the different AR variation methods, only the wing´s outer part (outside the kink) is modified. The inner part (from root to kink) remains the same in order not to affect the wing-fuselage mount and the engine-wing integration. The engines keep their absolute location. The leading-edge sweep remains unchanged. The control surfaces keep their relative coordinates. Therefore, the control surfaces will be stretched similar to the wing. The horizontal and vertical tail planes remain unchanged. Regarding the inner structure, the objective is to keep a constant spacing between the ribs. The number of ribs arises from 35 for the lowest AR to 38 for the highest AR. The rib layout and absolute y-values for the ribs up to the folding-rib (rib no. 28 in Figure 7) are kept constant for all variants. Additional ribs needed to keep a similar rib spacing, are placed aft of the folding-rib. Concerning the wing tip and especially the tip chord length, neither manufacturing constraint regarding space needed for actuators nor aerodynamic constraints regarding lift separation are considered. The DLR-F25 already has a narrow tip chord of *0.6 m*. For the highest within this study possible AR of *18.3* (17% higher than the baseline), the tip chord is *0.15 m*. Such a narrow tip is a challenge for the detailed aerodynamic design of the wing but is no part of this investigation. For all variants, the baseline twist at each section was kept the same and no twist correction has been performed to adapt the lift distribution.

4.1.1 Span Variation

The first concept consists on keeping the trailing edge lines constant and expand the span from *44 m* to *49 m*. The reference area will also grow but by less than five percent. The outer part modification is shown in Figure 15. The taper ratio diminishes with increased AR. For the span variation method, also a decrease in AR compared to the baseline has been performed.

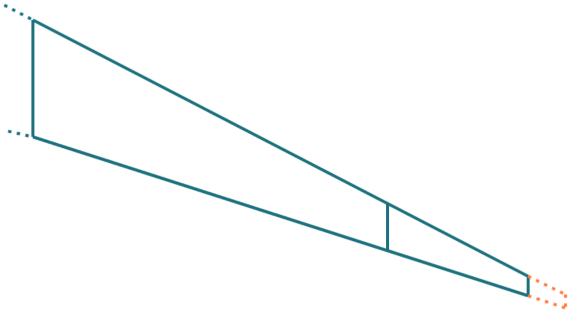

Figure 15: Schematic visualization of the AR-variation through 'span variation'.

4.1.2 Surface Variation

For the second method, the tip chord length is kept constant and the reference area gets up to five percent bigger. The trailing edge sweep angle slightly increases but not sufficient to really affect the quarter chord sweep angle. The taper ratio is constant for the surface variation concept. The modification is represented in Figure 16.

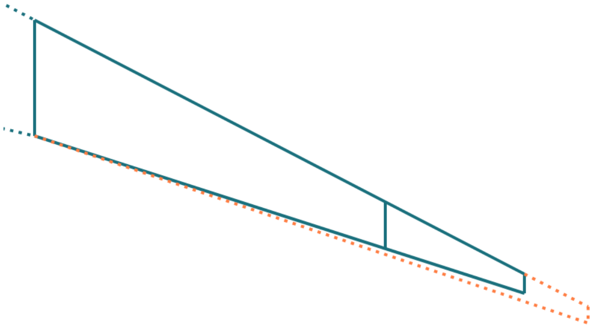

Figure 16: Schematic visualization of the AR-variation through 'surface variation'.

4.1.3 Tip Chord Variation

The third concept is composed of diminishing the tip chord and keeping the reference area constant. The trailing edge sweep angle decreases slightly with small impact on the quarter chord sweep. This method leads to the smallest taper ratio at highest AR and is visualized in Figure 17.

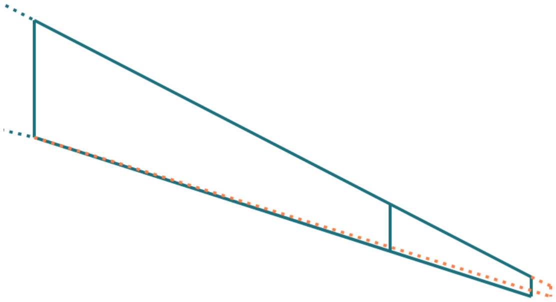

Figure 17: Schematic visualization of the AR-variation through 'tip chord variation'.

4.2 Results of the Aspect Ratio Variation

This paragraph highlights the effect of the aspect ratio variation on the main aircraft characteristics. The mass-dependent results within this chapter are presented for the OEM mass case only, since the results for the other mass cases are analogous. For the OEM case, the influence from different payload/fuel combinations among the AR variations can be neglected throughout the variants. To better understand the following results for the different variants of AR variation, first the effect of the main planform characteristics, which is especially important for the aerodynamics of the aircraft, are presented.

4.2.1 Effect on the Wing Planform

For the surface variation method, the tip chord is constant and the reference area grows by 5%. To achieve that change, the trailing edge sweep angle has to be enlarged. The span variation concept keeps the same sweep angle for the leading and trailing edge, while the reference area only enlarges by 2%. Moreover, for the tip chord variation, the reference area is constant.

On the left half of Figure 18, the effect on the MAC is visualized. For all the variation concepts, the MAC diminish, when the AR rises. This is due to the fact, that the wing is tapered and swept. It is not shown in a figure, but due to the fact of the backward sweep of the wing, the x-position of the MAC moves backwards for all three variants with bigger AR and the y-position of the MAC along the span moves outboard respectively, while the movements for the surface variation method are the largest. The movement and shrink of the MAC for the surface variation method is the largest, due to the taper ratio of the wing variants, as described below.

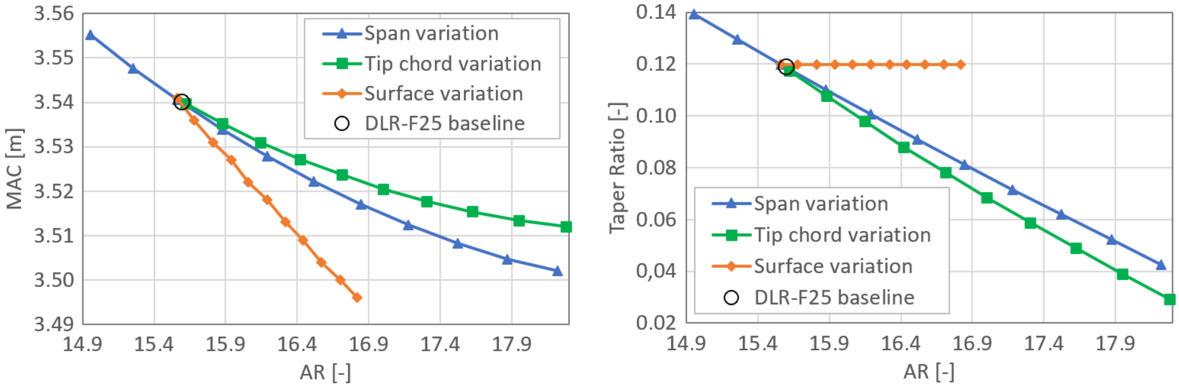

Figure 18: Variation of the mean aerodynamic chord (left) and the taper ratio (right) of the main wing as a function of the AR for the different AR variation concepts.

As highlighted in the introduction, the taper ratio is also an important value for the characteristic of a wing planform. The most AR variations in the literature try to keep as many other parameters of the planform constant, to not induce unwanted effects or counteract the effect of the change in AR. The taper ratio is only constant for the surface variation method, as shown in the right half of Figure 18. For the both other concepts, the taper ratio diminishes with increasing AR. Since the length of the wing´s root chord is constant for all variations, the changes in taper ratio come from the diminishing tip chord. And due to the shorter tip chord for the span variation and tip chord variation methods, the outer area of the wing is not enlarged as much for these both concepts compared to the surface variation, which shows the largest effect on the MAC.

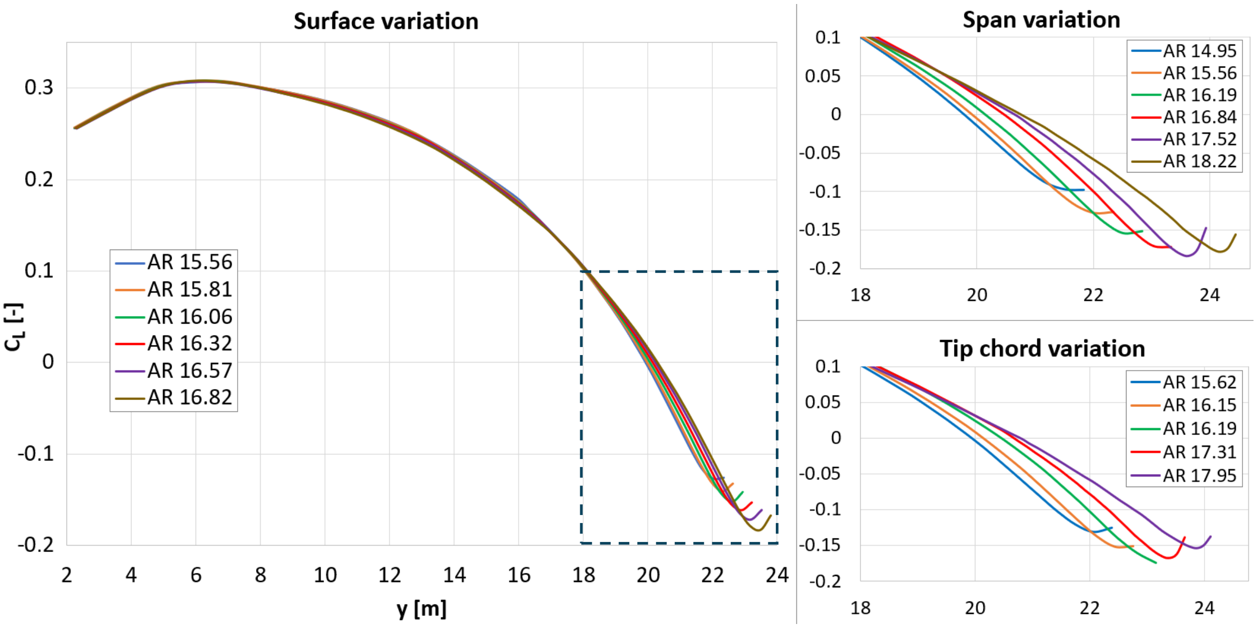

Figure 19. Distribution of the lift coefficient among the wing span for the different ARs of the OEM case for 1g-level flight of the surface variation method and augmented tip distribution for the span variation and tip chord variation concepts.

Since the twist is not corrected among the different AR variations to match the lift distribution of the baseline configuration, a bigger AR stretches the lift distribution as highlighted in Figure 19. The lift coefficient distribution is forming a bell-shape comparable to the in 1933 presented theory of Prandtl describing a lift distribution for optimal wing designs with a variable wing span. The negative tip twist is shifted more outboard with the growing AR, while the inner part of the wing´s lift coefficient stays unvaried. The resulting downforces at the wing tip grows and emphasize the washout-effect leading to a passive load alleviation for increased AR. Analogous effects on the loads are presented in Chapter 4.2.3.

4.2.2 Effect on the Longitudinal Stability

It is essential to check whether the aircraft is still stable in case the planform changes, especially for an increase in AR. As explained in Subsection 3.2.2, an aircraft is longitudinally stable if its stability margin is positive. The stability margin depends on the aircraft´s center of gravity (CG) and aerodynamic center. The effect of the AR variation for the different variations on the CG is shown in Figure 20 (left). Since the aircraft´s wing is swept backwards and the CG is placed with a target CG assignment, following the same percentage of the MAC as listed in Table 6 for each variant, the CG moves backwards (increased absolute x-position) with a bigger AR for the different variation concepts. As described, the effect on the MAC is the largest for the surface variation method and likewise the largest for the movement in CG position.

Figure 20 (right) shows the shift of the aerodynamic center with respect to the AR for the three different concepts. As the wing is backwards swept, the aerodynamic center moves backwards with growing AR for the surface variation method, because of the expanded surface at the outer part of the wing is shifting the center of area more outboard. The discontinuity in the results between AR *16.06* and *16.2* can be explained by the change of inner topology between the two variants. For the AR *16.2*, an additional rib is placed at the outboard section to fulfill the rib spacing constraint. For the span variation and the tip chord variation concepts, at first the aerodynamic center moves backwards and then, beyond an aspect ratio of *16.2*, moves forward again. That is due to the fact, that the outer wing section becomes less effective in generating lift in consequence of the shortened wing chord at the tip with the increased AR.

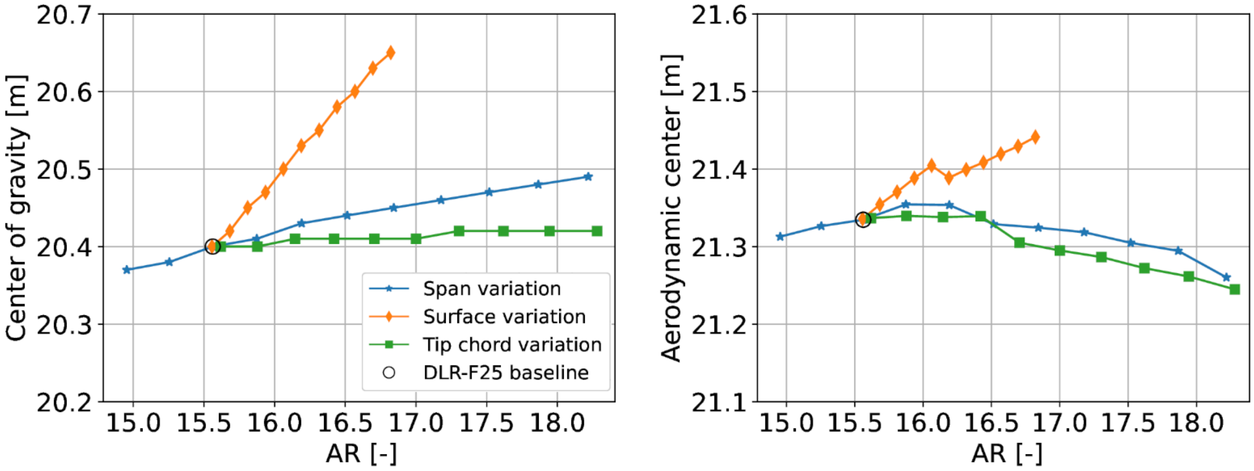

Figure 20: Variation of the aircraft´s x-position of the center of gravity (left) and x-position of the aerodynamic center (right).

The stability margin (see Figure 21) decreases for each mass case and method and is far away of becoming negative. The aircraft is always stable. The stability margin declines faster for the surface variation concept than for the other variation concepts. Once again, the variation of the reference area plays an important role in the results, this is why the constant surface variation has the smallest slope.

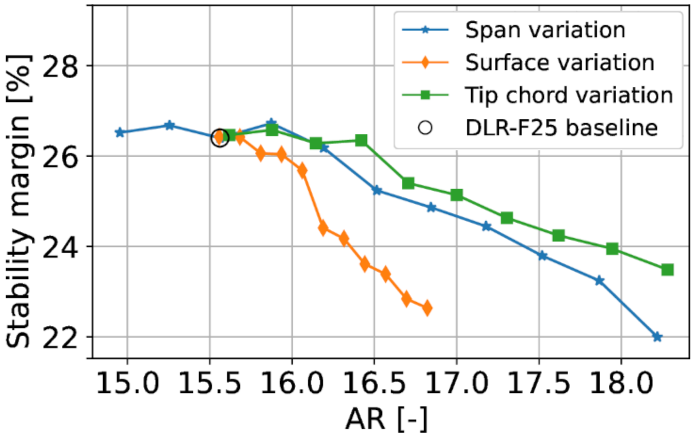

Figure 21: Variation of the aircraft´s stability margin as function of the AR for the OEM case.

4.2.3 Effect on the Loads

In Figure 22, the variation for the cutting loads of maximum bending and minimum torsion are visualized with respect to the AR. In the left half, the bending moment shows a comparable trend as for the aerodynamic center (see Figure 20, right). For the surface variation method, the maximum bending moment rises considerably with growing AR up to an AR of *16.06*. Then, an additional rib is placed in the model, leading to a different stiffness and mass distribution at the tip of the wing. That additional rib seems to mitigate the effect for the growing bending moment while the AR increases, since the ascent in wing bending moment becomes less for higher ARs. For the both variants with a declined taper ratio, the bending moment first rises with an increase in AR, while after an AR of *16.4*, the bending moments is declining and after the AR of *17.4*, the maximum bending moments are even less compared to that on the baseline configuration. That behavior can be explained by the bell-shaped lift distribution as highlighted in Figure 19. The resulting downforce on the wing tip due to the negative twist and arising washout-effect is shifting the upwards lift forces more inboard and consequently reduces its lever arm.

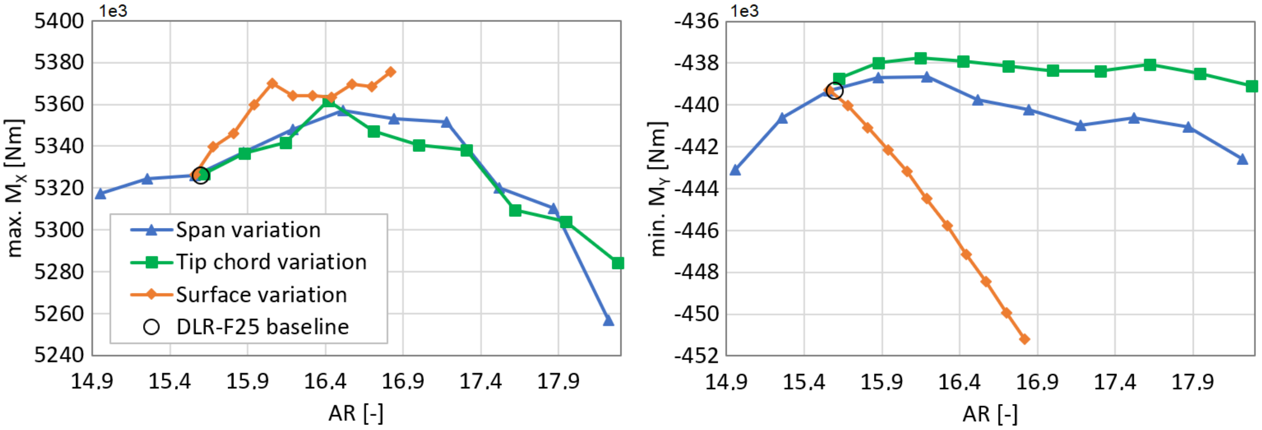

Figure 22: Variation of the cutting loads – maximum bending moment (left) and minimum torsional moment (right) as a function of the AR at the station *W640005* (see Figure 10).

The trend of the minimum torsional moment is visualized in the right half of Figure 22. The minimum (maximum negative) torsional loads grow the most (~2,4% deviation) with an increase in AR for the surface variation concept, while the span variation method deviates about 1% around the baseline configuration. A nearly constant (~0.3% deviation) minimum torsional moment results for the tip chord variation. The surface variation has a longer chord at the tip compared to the other variation concepts. The expanded area is placed behind the baseline wing due to the backwards shift of the trailing edge. That moves the center of pressure backwards with an increase in AR, leading to more negative torsional momentum.

4.2.4 Effect on the Structural Properties

One main driver for the weight of a wing is the maximum bending moment (M_x) near the wing´s root. Figure 23 represents the change in the operating empty mass obtained after the loads and mass of the wing components are converged within the iterative loop of cpacs-MONA. The operating empty mass is the sum of all aircraft structural mass components, system components and operational items. It is observed, that the mass for the surface variation method with its constant taper ratio and an enlargement in wing surface leads to a continuous growth of mass with increased AR. Although there is one more rib placed at the wing for the AR higher than *16.06*, the mass is not grown for the change in AR from *16.06* to *16.2*. Such behavior can be explained by the trend of the bending moment. The bending loads for the AR of *16.2* with the additional mass near the tip of the wing due to the additional rib leads to lower bending moments compared to the AR *16.06*. The span variation and tip chord variation show the same trend for the aircraft mass compared to the bending moments. The mass first rises up to an AR of *16.4* and decreases afterwards. The maximum take-off mass case is a design mass and kept constant for all variations of AR. The both other mass cases are the combination of the resulting operating empty mass and the payload/fuel combinations as listed in Table 5 and therefor show the same trend as the operating empty mass.

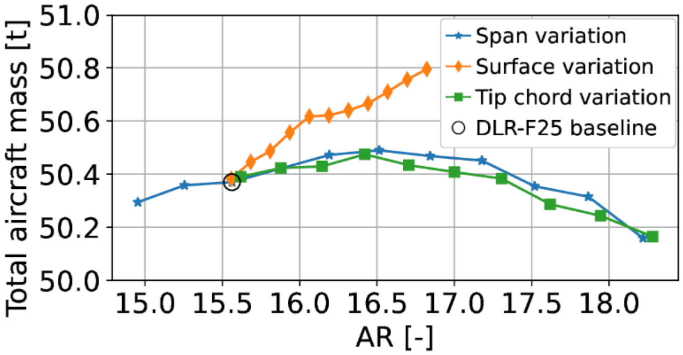

Figure 23: Variation of the aircraft´s operating empty mass as a function of the AR.

The elastic displacements of the wing in steady level flight are crucial for the aerodynamic design of the wing, since they represent the flight shape of the wing, where the aircraft operates most of the time during flight mission. Figure 24 illustrates the maximum vertical displacement (left) and minimum wing torsional (twist) displacement (right) emerging at the wing´s tip. Since the trend of displacement with respect to the AR is of interest, again the operating empty mass case in steady level flight is selected, although it is not representing an actual cruise condition or an aerodynamic design case. The variation in vertical and torsional tip displacement for the variation concepts with diminishing taper ratio is not varying much. The vertical displacement for the surface variation method constantly diminish with increased AR, while the negative twist deformation shows a declining trend.

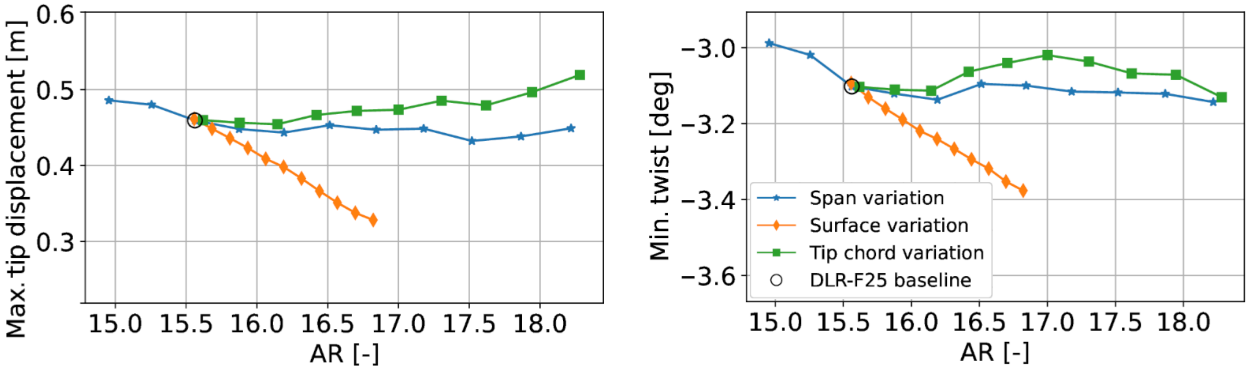

Figure 24: Variation of the maximum vertical wing tip displacement (left) and minimum wing torsional displacement (right) of the OEM mass case in steady level flight.

4.2.5 *Effect on the Aerodynamic Performance*

The aerodynamic performance can be analyzed with three different parameters. One parameter is the Oswald factor as a value describing how much the actual lift distribution differs from the elliptical lift distribution. Another performance indicator is the lift generated by the wing, that can be represented by the dimensionless lift coefficient. As a consequent of the lift, the induced drag coefficient is the third value of interest.

The evaluation of the Oswald factor with respect to the AR is shown for each method in the left side of Figure 25. Because the twist distribution is not adapted for the AR variation, for each investigated concept, the Oswald factor decreases with the increase of wing AR.

The lift coefficient for the three AR variation concepts is depicted in the right side of Figure 25 for the operating empty mass case at a Mach number of *0.82* in *8000 m* elevation. Since the wing surface area is one factor for the determination of the lift coefficient, there is only a small change in lift coefficient for the tip chord variation method, where the reference area is constant. The biggest change occurs for the surface variation concept, since that is the variant with the most change in wing reference area.

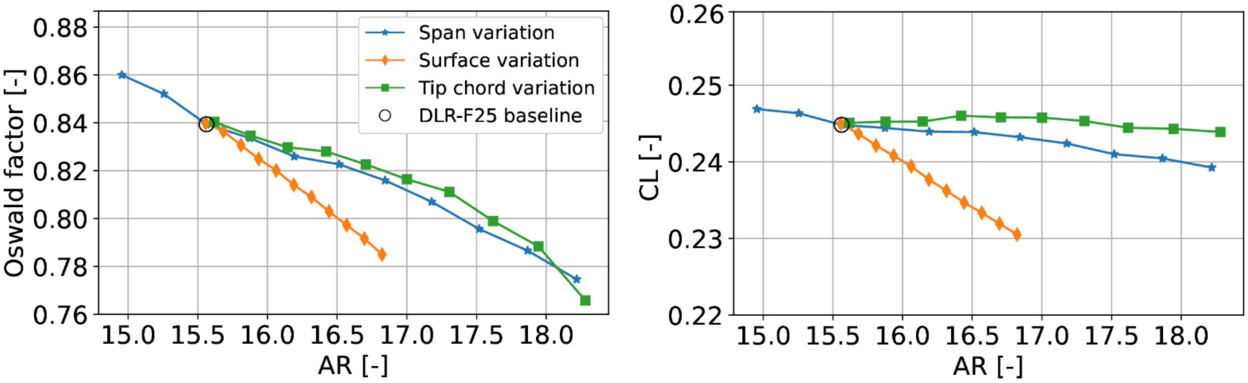

Figure 25: Variation of the Oswald factor (left) and lift coefficient (right) as function of the AR.

The most important parameter to obtain information about the fuel efficiency of the aircraft within this publication is the induced drag coefficient. As described within Paragraph 3.2.4, the induced drag coefficient can be calculated with the lift coefficient in the denominator, and the AR and the Oswald factor in the numerator. Figure 26 highlights the effect of the different AR variations on the induced drag coefficient. Because the AR grows faster than the Oswald factor is reduced (see Figure 25, left), the induced drag coefficient decreases for all variants with bigger AR. The lowest induced drag coefficient results for the surface variation concept, because here also the lift coefficient is reduced considerably with an increase of AR.

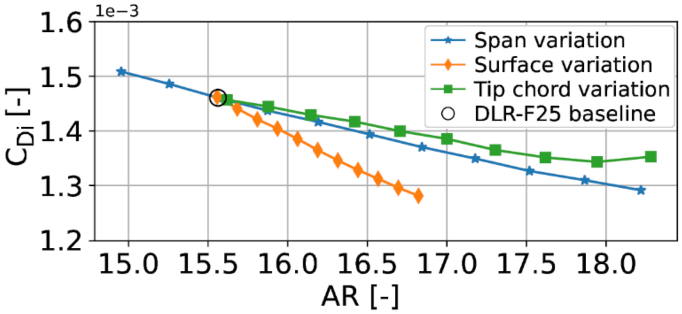

Figure 26: Variation of the induced drag coefficient as function of the AR.

5 SUMMARY AND CONCLUSIONS

Modern aircraft wings are complex structural components with highly sophisticated twist distributions, profile geometries and a kink position equipped with composite materials having direction-dependent stiffness distributions. They are therefore not straightforward describable in simplified analytical formulas. This work presents the effect of three different approaches to increase the AR of the DLR-F25 reference aircraft. The DLR-F25 is already equipped with a high-AR wing having an initial AR of *15.6*. Since the main goal of the variations was to not influence the wing-fuselage mount or the engine-wing integration, only the outer part of the wing has been adapted without the consideration of aerodynamic or manufacturing constraints. The so-called ‘surface variation’ method utilizes a constant taper ratio with a 5% enlargement of the wing surface area. The both other concepts have a decreased tip chord length leading to a reduced taper ratio with growing AR, while the ‘tip chord variation’ has a constant reference area and the ‘span variation’ slightly expand the reference area up to 2% compared to the baseline wing. For all variation concepts, the baseline twist distribution has been kept constant at the relevant wing sections and stretched for the different AR variants.

The automated aeroelastic structural preliminary design process cpacs-MONA has been used to set up the different global structural Finite-Element models of the AR variations to predict the effect of the AR on the loads, the structural properties and the aerodynamic performance. While the aeroelastic assessment is done using physics-based Finite-Element-Analyses, the aerodynamic performance is calculated with analytical formulations extracting required information from the simulation results.

The twist distribution of the baseline configuration leads to a so-called bell-shaped lift distribution resulting in a passive load alleviation effect, since the outer part of the wing produces less lift forces and therefore reduces the mass-driving maximum wing root bending moment. Since the twist is not adapted for the different AR variations, the effect of load alleviation is even elevated for the AR variation concepts with a diminishing trend in taper ratio, namely the span variation and the tip chord variation. The effect is so distinct, that the mass of the wing for higher ARs is even lower compared to the baseline configuration. The surface variation method shows the expected trend of growing mass with increased AR due to the fact of the constant taper ratio and the concurrent enlargement in surface area.

Regarding the aerodynamic performance, the induced drag coefficient declines for all variants with increased AR, since the AR expands faster than the Oswald factor decreases and therefore deviates from elliptical. The results presented in this paper emphasis the fact, that the elliptical lift distribution is not automatically the optimal distribution.

REFERENCES

[1] European Commission, "Flightpath 2050 : Europe’s vision for aviation : maintaining global leadership and serving society’s needs," Generaldirektion Mobilität und Verkehr, Generaldirektion Forschung und Innovation, Publications Office, https://data.europa.eu/doi/10.2777/50266, 2011.

[2] L. Prandtl, "Tragfluegel Theorie," in *Nachrichten von der Gesellschaft der Wissenschaften zu Goettingen*, Goettingen, Germany, Geschaeftliche Mitteilungen, 1918, pp. 451-477.

[3] L. Prandtl, "Ueber Tragfluegel kleinsten induzierten Widerstands," *Zeitschrift fuer Flugtechnik und Motorluftschiffahrt,* vol. Vol. 24, no. No. 11, pp. 305-306, 1933.

[4] W. F. Phillips, D. F. Hunsaker and J. D. Taylor, "Minimizing Induced Drag with Weight Distribution, Lift Distribution, Wingspan, and Wing-Structure Weight," in *AIAA Aviation Forum,* Dallas, Texas, United States of America, 2019.

[5] D. F. Hunsaker, W. F. Phillips and J. J. Joo, "Aerodynamic Shape Optimization of Morphing Wings at Multiple Flight Conditions," in *55th AIAA Aerospace Sciences Meeting; https://doi.org/10.2514/6.2017-1420,* Grapevine, Texas, United States of America, 9-13 January 2017.

[6] D. P. Raymer, Aircraft Design: A Conceptual Approach, Washington DC, United States of America: American Institute of Aeronautics and Astronautics, AIAA Education Series, 1989.

[7] M. Drela, Flight Vehicle Aerodynamics, United States of America: Massachusetts Institute of Technology, ISBN 978-0-262-52644-9, 2014.

[8] P. Hospodář, A. Drábek and A. Pracha, "Aerodynamic Design and Strength Analysis of the Wing for the Purpose of Assessing the Influence of the Bell-Shaped Lift Distribution," *Aerospace, MDPI, Special Issue: Multidisciplinary Multiobjective Design Optimization,* vol. 9, no. 13, p. https://doi.org/10.3390/aerospace9010013, 2021.

[9] T. R. Brooks, K. G. K. W. and M. J. R. R. A., "Benchmark Aerostructural Models for the Study of Transonic Aircraft Wings," *AIAA Journal,* vol. 56, no. 7, pp. 2840-2855, 2018.

[10] G. J. Kennedy, G. Kenway and J. R. R. A. Martins, "High Aspect Ratio Wing Design: Optimal Aerostructural Tradeoffs for the Next Generation of Materials," in *AIAA SciTech Forum,* National Harbor, Maryland, United States of America, 13-17 January 2014.

[11] D. E. Calderon, J. E. Cooper, M. Lowenberg, S. A. Neild and E. B. Coetzee, "Sizing High-Aspect-Ratio Wings with a Geometrically Nonlinear Beam Model," *Journal of Aircraft, American Institute of Aeronautics and Astronautics, Inc.,* vol. 56, no. 4, p. https://doi.org/10.2514/1.C035296, July 2019.

[12] F. Toffol and S. Ricci, "Preliminary Aero-Elastic Optimization of a Twin-Aisle Long-Haul Aircraft with Increased Aspect Ratio," *Aerospace, MDPI, Special Issue: Aircraft Design,* vol. 10, no. 372, p. https://doi.org/10.3390/aerospace10040374, 2023.

[13] T. Klimmek, "Parametrization of Topology and Geometry for the Multidisciplinary Optimization of Wing Structures," in *European Air and Space Conference,* 2009.

[14] MSC Software Corporation, MSC Nastran 2021 Quick Reference Guide, United States of America: HEXAGON, 8. Dec. 2020.

[15] M. Schulze, J. Neumann and T. Klimmek, "Parametric Modelling of a Long-Range Aircraft under Consideration of Engine-Wing Integration," *Aerospace,* Vols. Special Issue Aeroelasticity, Volume II, pp. 8(1), 2, 2021.

[16] T. Klimmek, M. Schulze, M. Abu-Zurayk, C. Ilic and A. Merle, "cpacs-MONA – An Independent and in High-Fidelity Based MDO Tasks Integrated Process for the Structural and Aeroelastic Design of Aircraft Configurations," in *IFASD*, Savannah, USA, 2019.

[17] M. Schulze, T. Klimmek, F. Torrigiani and T. F. Wunderlich, "Aeroelastic Design of the oLAF Reference Aircraft Configuration," in *Deutsche Luft- und Raumfahrtkongress (DLRK)*, Bremen, Germany (virtual), 2021.

[18] T. Klimmek, M. Schulze and S. Wöhler, "Investigation on Aeroelastic Characteristics due to Structural and Geometrical Variations for an SMR Aircraft Configuration using cpacs-MONA," in *Deutscher Luft- und Raumfahrt Kongress (DLRK)*, Stuttgart, Germany, 2023.

[19] M. Abu-Zurayk, A. Merle, C. Ilic, J. M. Feldwisch, M. Schulze, J. Häßy, M. De Lozzo, F. Gallard and A. Gazaix, "Comparing Two Multidisciplinary Optimization Formulations of Trimmed Aircraft Subject to Industry-relevant Loads and Constraints," in *AIAA AVIATION Forum; doi: 10.2514/6.2021-3075; ISBN 978-162410610-1*, Washington DC, United States of America, 2021.

[20] S. Görtz, M. Abu-Zurayk, C. Ilic, T. F. Wunderlich, M. Schulze, C. Kaiser, Ö. Süelözgen, A. Schuster, S. Dähne, M. Petsch, J. Häßy, S. Gottfried, R. Mischke, P. Knechtges and J. Hartmann, "Collaborative high fidelity and high performance computing-based MDO strategies applied to transport aircraft design," in *2nd European Workshop on MDO for Industrial Applications in Aeronautics*, Toulouse, France, 2019.

[21] C. Ilic, A. Merle, A. Ronzheimer, M. Abu-Zurayk, J. Jepsen, M. Leitner, M. Schulze, A. Schuster, M. Petsch and S. Gottfried, "Cybermatrix: A novel approach to computationally and collaboration intensive MDO for transport aircraft design," in *21st STAB/DGLR Symposium on New Results in Numerical and Experimental Fluid Mechanics*, Darmstadt, Germany, Springer, 2020, pp. 37-47.

[22] S. Görtz, C. Ilic, J. Jepsen, M. Leitner, M. Schulze, A. Schuster, J. Scherer, R.-G. Becker, S. Zur and M. Petsch, "Multi-Level MDO of a Long-Range Transport Aircraft Using a Distributed Analysis Framework," in *AIAA*, Denver, Colorado, USA, 2017.

[23] M. Alder, E. Moerland, J. Jepsen and B. Nagel, "Recent Advances in Establishing a Common Language for Aircraft Design with CPACS," in *Aerospace Europe Conference*, Bordeaux, France, 25. - 28. Feb. 2020.

[24] G. P. Chiozzotto, "CDloads: Conceptual design loads estimation.," DLR - Institute Of Aeroelastcity, Goettingen, Germany, 2013.

[25] F. van Dalen, "MDO load analysis and preliminary sizing," Delft University of Technology, Delft, Netherlands, December 1996.

[26] R. J. Guyan, "Reduction of Stiffness and Mass Matrices," *AIAA Journal,* vol. 3, p. 380, 1964.

[27] F. A. Administration, *Federal Aviation Regulations Part 25 C, Airworthiness Standards: Transport Category Airplanes,* 2010.

[28] MSC Software Corporation, MSC Nastran 2021 Aeroelastic Analysis User's Guide, United States of America: HEXAGON, 27. Nov. 2020.

[29] V. Handojo, "Contribution to Load Alleviation in Aircraft Pre-design and Its Influence on Structural Mass and Fatigue. DLR-Forschungsbericht. FLR-FB-2020-47. Dissertation.," Technische Universität Berlin, 2021.

[30] MSC Software, MSC Nastran 2017 Design Sensitivity and Optimization User's Guide, United States of America, 2016.

[31] DLR Institute of Aerodynamics and Flow Technology, "Virtual design environment for real, efficient engineering," [Online]. Available: https://www.dlr.de/de/as/forschung-transfer/projekte/virenfrei. [Accessed 21 May 2024].

[32] D. Scholz, "DataMorichon," 02 01 2008. [Online]. Available: https://www.fzt.haw-hamburg.de/pers/Scholz/arbeiten/DataMorichon.xls. [Accessed 02 05 2024].

[33] G. Schewe and H. Mai, "Influence of flexibility on the steady aeroelastic behavior of a swept wing in transonic flow," in *Journal of Fluids and Structures*, ISSN 0889-9746, Elsevier, 2018, pp. 255-269.

[34] E. Torenbeek, Advanced Aircraft Design - Conceptual Design, Analysis and Optimization of Subsonic Civil Airplanes, United Kingdom: John Wiley & Sons, 2013.

[35] S. G. Hedman, "Vortex Lattice Method for Calculation of Quasi Steady State Loadings on Thin Elastic Wings, Technical Report 105," October 1965.

[36] E. Albano and W. P. Rodden, "A Doublet-Lattice Method for Calculating Lift Distributions on Oscillating Surfaces in Subsonic Flow," *AIAA Journal,* 1969.

[37] J. D. Anderson, Fundamentals of Aerodynamics, United States of America: McGraw-Hill, Inc., ISBN 0-07-001679-8, 2017.

[38] R. M. Bogenfeld, S. Freund, S. Dähne, T. Wunderlich and T. Wille, "Damage Tolerance Allowable Calculation for the Aircraft Design with Static Ultimate Load," *Composite Structures,* vol. 329, no. ISSN 0263-8223, p. doi: 10.1016/j.compstruct.2023.117803, 2023.

COPYRIGHT STATEMENT

The authors confirm that they, and/or their company or organisation, hold copyright on all of the original material included in this paper. The authors also confirm that they have obtained permission from the copyright holder of any third-party material included in this paper to publish it as part of their paper. The authors confirm that they give permission, or have obtained permission from the copyright holder of this paper, for the publication and public distribution of this paper as part of the IFASD 2024 proceedings or as individual off-prints from the proceedings.